The Astrophysical Journal, 931:42 (8pp), 2022 May 20 https://doi.org/10.3847/1538-4357/ac5b79

Generating Stellar Obliquity in Systems with Broken Protoplanetary Disks

Marguerite Epstein-Martin[1,2], Juliette Becker[1], and Konstantin Batygin[1]
[1] Division of Geological and Planetary Sciences, California Institute of Technology, Pasadena, CA 91125, USA
[2] Department of Astronomy, Columbia University, 550 West 120th Street, New York, Ny 10027, USA
Received 2021 August 31; revised 2022 February 16; accepted 2022 March 4; published 2022 May 23

Abstract

Recent advances in submillimeter observations of young circumstellar nebulae have opened an unprecedented window into the structure of protoplanetary disks that has revealed the surprising ubiquity of broken and misaligned disks. In this work, we demonstrate that such disks are capable of torquing the spin axis of their host star, representing a hitherto unexplored pathway by which stellar obliquities may be generated. The basis of this mechanism is a crossing of the stellar spin precession and inner disk regression frequencies, resulting in adiabatic excitation of the stellar obliquity. We derive analytical expressions for the characteristic frequencies of the inner disk and star as a function of the disk gap boundaries and place an approximate limit on the disk architectures for which frequency crossing and the resulting obliquity excitation are expected, thereby illustrating the efficacy of this model. Cumulatively, our results support the emerging consensus that significant spin–orbit misalignments are an expected outcome of planet formation.

Unified Astronomy Thesaurus concepts: Planetary system formation (1257); Planet formation (1241); Protoplanetary disks (1300); Pre-main sequence stars (1290); Pre-main sequence (1289); Stellar accretion disks (1579)

1. Introduction

The standard picture of planet and star formation holds that planetary systems are born in a disk, yielding an initially common plane. This theory is validated by the near-alignment of our own solar system and numerous multitransiting exoplanet systems and has remained largely unaltered since its conception by Kant and Laplace in the 18th century (Kant 1755; Laplace 1796). A natural logical extension is to assume that the coincidence of angular momentum vectors extends to stellar spin axes.

The soaring number of exoplanet discoveries over the past two decades (Borucki et al. 2010, 2011; Howell et al. 2014; Guerrero et al. 2021) and the wide diversity of systems represented has, however, required a reevaluation of the one-size-fits-all paradigm. In particular, measurement of misalignment between stellar spin axis and planetary orbit, otherwise known as stellar obliquity, has increasingly fallen within the reach of the Rossiter–McLaughlin effect (McLaughlin 1924; Rossiter 1924; Winn et al. 2005), as well as other techniques (see review by Winn & Fabrycky 2015). Current measurements suggest that obliquities are common, particularly in systems hosting short-period planets orbiting stars hotter than the Kraft break (Winn et al. 2010; Morton & Winn 2014).

The dominant source of stellar obliquities remains controversial. Postformation perturbations due to planet–planet scattering (Ford & Rasio 2008; Nagasawa et al. 2008; Beaugé & Nesvorný 2012), Kozai–Lidov cycling (Wu & Murray 2003; Fabrycky & Tremaine 2007; Naoz et al. 2011), and chaotic interactions with additional planets in the system (Lithwick & Wu 2012) have all been proposed as plausible misalignment pathways. Alternative explanations, disrupting the established disk–star alignment paradigm, assert that obliquities may be excited prior to or in concert with planet formation. For example, the nonaxisymmetric collapse of the molecular cloud core has been shown to create stellar obliquities (Tremaine 1991; Bate et al. 2010), as has interactions between the stellar magnetosphere and disk (Lai et al. 2011).

Of particular relevance to this work is a distinct process: the binary–disk torquing mechanism for exciting spin–orbit misalignments (Batygin 2012; Batygin & Adams 2013; Spalding & Batygin 2014; Lai et al. 2018). Within the framework of this model, spin–orbit misalignments are induced by a stellar companion that torques the nebula, resulting in nodal regression. Simultaneously, the nebula torques the star, driving nodal regression of the stellar spin axis. As the nebula dissipates and the primary star contracts, a commensurability between the regressing disk and precessing stellar spin axis ensues, and the system evolves through a resonant encounter. This encounter leads to impulsive excitation of the stellar obliquity, replicating the full obliquity range. Operation of this mechanism is best exemplified by the recent discovery of K2-290 A, a star whose spin is tilted 124° with respect to the orbits of both of its known planets, with a binary companion capable of tilting the protoplanetary disk (Hjorth et al. 2021).

Previous work toward understanding stellar obliquity with respect to short-period planets has generally treated disks as rigid objects, where rigidity means equal inclinations and precession of the nodes for all disk annuli. However, recent observations of protoplanetary disks show evidence for disks containing wide gaps with misalignments between the inner and outer components. To this end, Brauer et al. (2019) observed shadows cast by misalignment between inner and outer disks; Ansdell et al. (2020) observed "dipper" transit systems and found that often, the inner disk causing the dipper appears to be misaligned with an outer component visible with the Atacama Large Millimeter/submillimeter Array (ALMA); and Francis & van der Marel (2020) used images of inner and outer disks to study the brightness profiles and identify additional misaligned systems. In fact, of all systems where

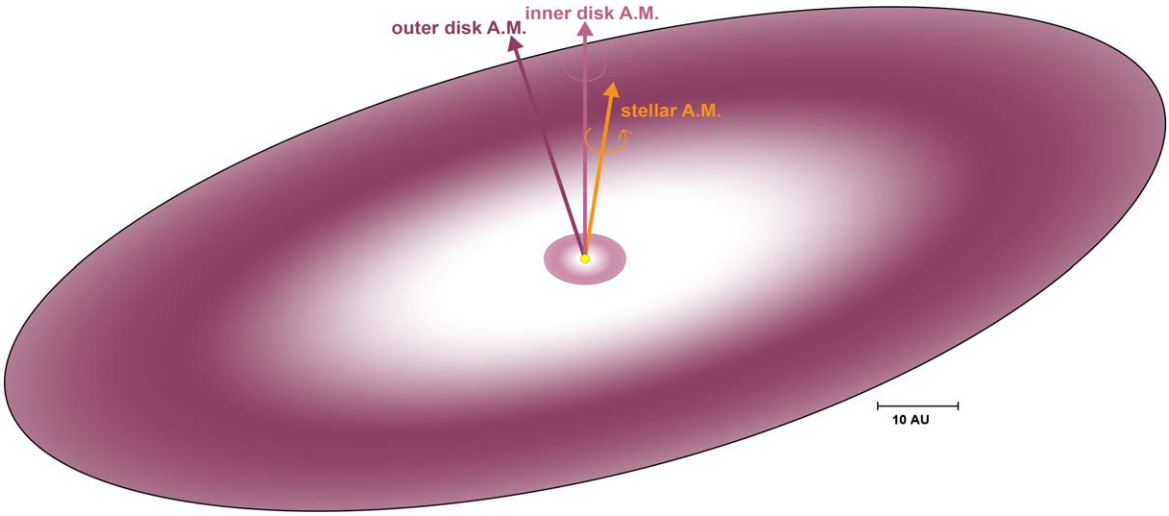

Figure 1. Schematic of the system geometry under consideration in this work, which includes three distinct components: a central star, an inner disk, and an outer disk. Misalignment in angular momenta may exist between any components in the system, and the precession of the star is driven by the effectively static potential of the outer disk and the time-varying potential of the inner disk.

both inner and outer disk components can be resolved by ALMA (Francis & van der Marel 2020), roughly 85% of the protoplanetary disks exhibit some misalignment or indirect evidence of misalignment (such as warps, shadows, or a dipper host). Such misalignments can be caused by massive planets (Nealon et al. 2018; Zhu 2019) forming in the disk or a stellar binary companion (Facchini et al. 2018).

While presenting a complicating detail to the previously mentioned explanations of stellar obliquity, the dynamical evolution of a broken, misaligned disk can be analyzed in much the same way as the binary–disk torquing scenario. That is, the outer, misaligned disk is qualitatively analogous to a binary companion, acting as a time-dependent outer potential influencing the inner disk–star orientation. A schematic of the relevant geometry of the system is included in Figure 1. Accordingly, in this work, we investigate the possibility of disk–disk torquing producing stellar obliquities independently, without invocation of a binary companion.

We ground our analysis in the framework of secular theory using the angular momentum arguments in Section 2 to support a simplified analytical model demonstrating that back-reactions of the star upon the inner disk and the inner disk upon the outer disk can be neglected. In Section 3, we derive the characteristic precession timescales for the inner disk and stellar spin axis. We use these expressions in Section 4 to define the disk structure criteria for obliquity excitation and demonstrate the efficacy of this mechanism with numerical integrations. In Section 5, we conclude and note avenues for future study.

2. Angular Momentum Distribution in the Star–Disk–Disk System

To determine the relevant dynamics, we will first consider the hierarchy of angular momentum in the star–broken disk system. By comparing the angular momentum for the star, inner disk, and outer disk, we can determine which component drives which and demonstrate that back-reactions can be neglected in this analysis. We note that this angular momentum argument holds provided that the effects of bending waves, viscosity, and disk self-gravity are sufficiently strong that the successive radial components of the disk remain coupled to each other (Batygin 2012; Lai 2014; Zanazzi & Lai 2018). In this case, the individual disk components may be treated as effectively rigid, an assumption that is expected for typical protoplanetary disk parameters (Larwood et al. 1996; Batygin et al. 2011; Zanazzi & Lai 2018).

As is typically done in the literature, for the protoplanetary disk, we will assume a surface density function of the type

$$\Sigma = \Sigma_0 (a_0/a)^p. \tag{1}$$

In Equation (1), a_0 is a reference radius, Σ_0 is the surface density at radius a_0, and p is the power-law index of the surface density profile. For definitiveness, we assume $p = 1$ (Mestel 1963; Andrews et al. 2009). Although the disk considered in this work has a gap separating the misaligned inner and outer components, we assume that when the disk is present, it obeys the above surface density profile.

To find the angular momenta of the two disk components, we first specify the angular momentum of a infinitesimal annulus,

$$d\mathcal{L} = \sqrt{GMa}\, dm, \tag{2}$$

where G is the gravitational constant, M is the mass of the central star, and $dm = 2\pi\Sigma a da$ is the mass enclosed by the ring of width da and mean orbital distance a. With this identity in mind, we take the disk to be made up of a series of infinitesimal annuli such that the expression for the angular momentum of the disk component can be written

$$\mathcal{L} = \int_{a_{\rm inner}}^{a_{\rm outer}} 2\pi \sqrt{GMa}\ \Sigma_0\ (a_0/a)\ a da, \tag{3}$$

where $a_{\rm inner}$ and $a_{\rm outer}$ denote the inner and outer radii of the disk component under consideration. Similarly, we can write an expression for the angular momentum of the central star,

$$\mathcal{L}_* = I_0 M R^2 \Omega, \tag{4}$$

where I_0 denotes the numerical coefficient of the stellar moment of inertia, R is the stellar radius, and Ω is the stellar rotational frequency.

Naturally, a young, disk-bearing system can be expected to undergo a physical transformation over the course of the disk and stellar pre-main sequence lifetime. Thus, we cannot necessarily take the comparative relationships between the stellar, inner disk, and outer disk angular momenta (i.e., $\mathcal{L}_{\rm d,out} > \mathcal{L}_{\rm d,in} > \mathcal{L}_{*}$) as a given. It is thus worthwhile to examine the time dependence of the components of angular momenta over the course of the system evolution.

The T Tauri stars with which we are concerned contract on a Kelvin–Helmholtz timescale as they proceed along their Hayashi track. Using a polytropic model to specify the stellar properties, the stellar radius is expected to evolve as (Chandrasekhar 1939)

$$R_{\star} = R_{\star}^{0}\left[1 + \left(\frac{5-n}{3}\right)\frac{24\pi\sigma T_{\rm eff}^{4}}{GM(R_{\star}^{0})^{3}}t\right]. \quad (5)$$

For a fully convective star emerging from the embedded phase and evolving along the Hayashi track, a polytropic index $n = 3/2$ is appropriate. Here $R_{\star}^{0}$ is the stellar radius at an initial time $t = 0$, approximately 0.1–0.5 Myr since the stellar birth. A star of mass $M = 1\ M_{\odot}$ is expected to have an initial radius $R_{\star}^{0} \approx 4R_{\odot}$, evolving according to Equation (5) with effective temperature $T_{\rm eff} = 4100$ K (Siess et al. 2000).

The other physically evolving parameter we must consider here is the mass of the inner and outer disk, which will decrease with time. Here we follow Laughlin et al. (2004) and use a simple dissipation model for both disk components, varying mass with time as

$$M_{\rm disk} = \frac{M_{\rm disk,\,0}}{1 + t/\tau_{\rm acc}}. \quad (6)$$

A reasonable fit to the observations, consistent with the work of Hartmann (2008), Herczeg & Hillenbrand (2008), and Hillenbrand (2008), is achieved by setting the accretion timescale to $\tau_{\rm acc} = 0.5$ Myr and the initial surface density profile of the disk by Equation (1) with $a_0 = 1$ au and $\Sigma_0 = 2 \times 10^3$ g cm^{-2}.

To complete our calculation, we must define the radial bounds over which we integrate for both the inner and outer disks. The interior boundary of the inner disk is determined self-consistently by noting that T Tauri magnetic fields of approximately a kilogauss are expected to disrupt the conductive nebular fluid near the star, carving out a cavity in the inner disk. The radial extent of this disruption can be derived in several ways, all approximately yielding the same scaling but most straightforwardly understood by equating the stellar magnetic pressure to the ram pressure of infalling disk material (Ghosh & Lamb 1978; Armitage 2020). The result determines the interior disk edge, also known as the Alfvén radius:

$$a_{\rm x} = \Pi\left(\frac{8\pi^2}{\mu_0^2}\frac{\mathcal{M}^4}{GMM_{\rm d}^2}\right)^{1/7}. \quad (7)$$

Here Π is a dimensionless constant of order unity, $\mathcal{M}$ is the stellar magnetic moment, and $\dot{M}_{\rm d}$ is the mass accretion rate onto the central star. Because higher-order components of the stellar magnetic field drop off steeply with radius, the magnetic moment is well approximated by a dipolar field ($\mathcal{M} = B_{\rm dip}R_{\star}^{3}/2$). For typical T Tauri parameters, the theoretically expected location of the interior disk edge $_{\rm ax}$ will range between 0.05 and 0.2 au (Shu et al. 1994).

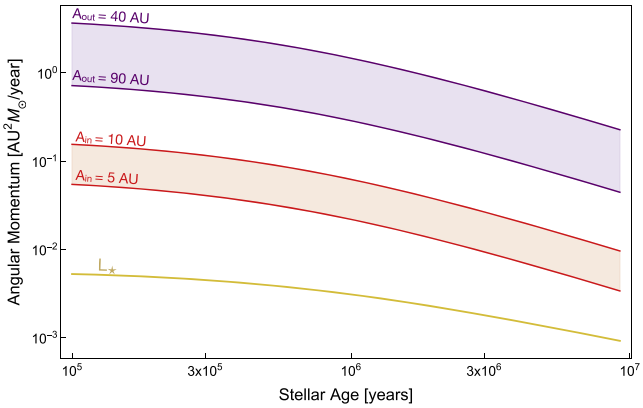

Figure 2. Angular momentum over time for three components: a range of possible values for the inner disk in purple, with an outer edge ranging from 5 to 10 au; an outer disk, denoted in red, with an inner edge varying between 40 and 90 au; and a solar-mass star in yellow. Within the time that the disk is expected to be present in the system, the hierarchy of angular momentum described in Section 2 is expected to hold for this typical architecture.

Assuming the outer disk extends to ∼100 au, we are left to define only the radial extent of the disk gap. We take these from observations by Ansdell et al. (2020) and Francis & van der Marel (2020) that find that, on average, the interior gap edge $A_{\rm in} \sim 5$ au and the outer gap edge $A_{\rm out} \sim 50$ au.

Throughout the evolution of the system shown in Figure 2, there emerges a clear hierarchy in the angular momenta, which can thus be written as follows:

$$\mathcal{L}_{\rm d,out} \gg \mathcal{L}_{\rm d,in} \gg \mathcal{L}_{*}, \quad (8)$$

where the difference between each angular momentum generally constitutes an order of magnitude.

Satisfaction of Equation (8) allows us to adopt a simplified mathematical relationship between the three components. The outer disk component, with the largest angular momentum, will essentially serve as a static potential on the inner two components. In turn, the inner disk will be torqued only by the outer disk component, and the star will be torqued in turn by the inner disk. It is important to note that violation of this assumption would force more complex dynamical behavior, including back-reactions of interior components on exterior components.

3. Gravitational Torques

The angular momentum arguments of the previous section illustrate that the dynamics of the broken disk–star system are fundamentally analogous to the gravitational interaction between a star, an intact disk, and a companion discussed elsewhere (Batygin 2012; Batygin & Adams 2013; Spalding & Batygin 2014; Lai et al. 2018). Nevertheless, a key distinction in the governing dynamics arises from the time dependence of the outer disk's mass. As in the binary–disk model, we adopt a Hamiltonian framework in describing the system dynamics. Because this model is well developed in other works, we focus our attention on the characteristic frequencies, namely, the precession rate of the inner disk and stellar axis, which are unique to the broken disk setup. For a more detailed description of the Hamiltonian geometry, we refer the reader to the works cited above.

3.1. Disk Precession

To begin, we consider the gravitational response of the inner disk to a misaligned outer disk. As in Section 2, we approach the inner and outer disks as a series of infinite annular wires whose dynamical interactions are limited to the idealized case where viscosity, bending waves, and self-gravity are sufficiently large that the disk remains coupled and coplanarity is maintained among neighboring annuli.

Taking advantage of the smallness of the inner disk relative to the outer disk, we adopt a Kaula-type expansion of the Hamiltonian using the semimajor axis ratio ($a_{\rm in}/a_{\rm out}$) as an expansion parameter. Note that an expansion of this type is consistent with the aforementioned angular momentum hierarchy and places no restriction on the mutual inclination of the inner and outer disks. To quadrupole order, the Hamiltonian is written (Kaula 1962; Mardling 2010)

$$\mathcal{H}_{\rm wire} = \frac{G}{4}\frac{dm_{\rm in}dm_{\rm out}}{a_{\rm out}}\left(\frac{a_{\rm in}}{a_{\rm out}}\right)^2\left[\frac{1}{2}(3\cos^2(i_{\rm in}) - 1)\right], \quad (9)$$

where $i_{\rm in}$ is the inclination of the inner disk, and we have aligned our frame of reference with the plane of the outer disk such that $i_{\rm out} = 0$.

Although the Keplerian orbital elements are widely understood and readily interpretable, they do not constitute a canonically conjugated set of coordinates. In order to solve for the evolution of the system by way of Hamilton's equations, we must introduce an alternate, canonical coordinate system, namely, the scaled Poincaré action-angle coordinates:

$$Z_{\rm in} = 1 - \cos(i_{\rm in}), \qquad z_{\rm in} = -\Omega_{\rm in}. \quad (10)$$

Because these are not the standard Poincaré coordinates but are scaled by the angular momentum of an annulus ($d\Lambda_{\rm in} = dm_{\rm in}\sqrt{GMa_{\rm in}}$), for the Hamiltonian to remain canonical, it must be similarly scaled. After substituting coordinates and scaling, the new scaled Hamiltonian becomes

$$\tilde{\mathcal{H}}_{\rm wire} = \frac{\mathcal{H}_{\rm wire}}{d\Lambda_{\rm in}} = \frac{3}{4}\sqrt{\frac{GM}{a_{\rm in}^3}}\frac{dm_{\rm out}}{M}\left(\frac{a_{\rm in}}{a_{\rm out}}\right)^3\left(Z_{\rm in} - \frac{Z_{\rm in}^2}{2}\right). \quad (11)$$

Note, however, that Equation (11) models only the gravitational forcing due to an outer disk annulus and fails to account for the radial extent of the outer disk. The potential of the full outer disk is modeled by integrating the Hamiltonian radially from the outermost edge of the disk to the outer edge of the disk gap ($A_{\rm out}$),

$$\tilde{\mathcal{H}} = \int_{A_{\rm out}}^{\infty}\tilde{\mathcal{H}}_{\rm wire} = \frac{3\pi}{4}\sqrt{\frac{GM}{a_{\rm in}^3}}\frac{\Sigma_0 a_0 a_{\rm in}}{M}\left(\frac{a_{\rm in}}{A_{\rm out}}\right)^2\left(Z_{\rm in} - \frac{Z_{\rm in}^2}{2}\right), \quad (12)$$

where we have used the stiff dependence of Equation (11) on $a_{\rm out}$, integrating the outer disk radially from infinity so that we can define the outer disk by the outer gap edge ($A_{\rm out}$) only. For a disk extending to ~100 au, this amounts to a correction factor of <1% and can be neglected for the purposes of this work.

Critically, the Hamiltonian in Equation (12) has no $z_{\rm in}$ dependence. From Hamilton's equations, we understand this to mean that the inclination of the inner disk is constant in time, and the longitude of the ascending node of an inner disk annulus regresses at a constant rate, $dz_{\rm in}/dt$, calculated as

$$\frac{dz_{\rm in}}{dt} = \frac{\partial\tilde{\mathcal{H}}}{\partial Z_{\rm in}} = \frac{3\pi}{4}\sqrt{\frac{GM}{a_{\rm in}^3}}\frac{\Sigma_0 a_0 a_{\rm in}}{M}\left(\frac{a_{\rm in}}{A_{\rm out}}\right)^2(1 - Z_{\rm in}). \quad (13)$$

To find the rate of nodal recession for the entire inner disk, we approximate the mass,

$$m_{\rm in} = \int_{a_{\rm x}}^{A_{\rm in}} 2\pi\Sigma_0 a_0 da_{\rm in} \approx 2\pi\Sigma_0 a_0 A_{\rm in}, \quad (14)$$

under the assumption that the inner disk has a significant radial extent ($a_{\rm X} \ll A_{\rm in}$). The rate of nodal precession may be derived by taking the orbital angular momentum weighted average of the forced recession rates of the individual disk annuli:

$$\omega = \frac{\int_{a_{\rm X}}^{A_{\rm in}}\frac{dz_{\rm in}}{dt}2\pi\Sigma_0 a_0\sqrt{GMa_{\rm in}}da_{\rm in}}{\int_{a_{\rm X}}^{A_{\rm in}}2\pi\Sigma_0 a_0\sqrt{GMa_{\rm in}}da_{\rm in}} = \frac{-3}{16}\sqrt{\frac{GM}{A_{\rm in}^3}}\frac{m_{\rm in}}{M}\left(\frac{A_{\rm in}}{A_{\rm out}}\right)^2\cos(i_{\rm in}). \quad (15)$$

The result is that the nodal precession of the entire disk (ω) differs from an annulus at the outer edge of the inner disk by a factor of 1/2.

Although our approach is distinct, Equation (15) is analogous to Equation (19) in Larwood et al. (1996), where the precession frequency was derived by dividing the total torque acting on the inner disk by the disk's angular momentum. Notably, by assuming a consistent density profile between the inner and outer disks, Equation (15) does not explicitly include the mass of the outer disk forcing the inner disk. Despite this somewhat less intuitive formulation, Equation (15) has the advantage of describing the dynamics of the inner disk forced by the outer disk by the boundaries of the disk gap only.

Bear in mind, Equation (15) applies only if the inner disk precesses as a rigid body. That is, inclination ($i_{\rm in}$) and node ($\Omega_{\rm in}$) are consistent between disk annuli. This assumption is appropriate so long as the disk precession timescale exceeds the time for sound waves to propagate through the disk, or $(c_s(r)/r) > \omega$, where $c_s(r)$ is the sound speed in the disk at radius r (Larwood et al. 1996). For a thin, flat disk, $c_s \propto r^{-3/8}$ (Armitage 2020), and the lower bound $c_s(r = 10\ {\rm au})/10\ {\rm au} \approx 4 \times 10^{-10}$ is over 3 orders of magnitude larger than the largest precession frequency (ω) relevant here. Thus, we can safely assume the disk precesses as a rigid body and proceed with our analysis.

3.2. Stellar Spin Axis Precession

For the sake of simplicity, we model the rotational deformation of the central star as a point mass surrounded by a circular wire. To quadrupole order, these two systems can be considered mathematically equivalent so long as their moments of inertia and gravitational potentials are consistent. The quadrupolar potential of a rotationally deformed spheroid is

$$V_{\rm quad} = \frac{GM}{r}J_2\left(\frac{R}{r}\right)^2\mathcal{P}_2(\cos(\theta)), \quad (16)$$

where $\mathcal{P}_2(\cos(\theta))$ is a Legendre polynomial of degree 2, and the angle $\boldsymbol{\theta}$ is measured from the stellar spin axis (Section 4.5 of Murray & Dermott 1999). The $\boldsymbol{J}_2$ is a dimensionless constant used here in its approximate form,

$$\boldsymbol{J}_2 = \frac{\Omega^2 R^3}{3GM} k_2, \tag{17}$$

where $\boldsymbol{k}_2$ is the stellar Love number. Setting the potential of the hoop to Equation (16) and the moment of inertia to $\boldsymbol{I}_0 \boldsymbol{M}\boldsymbol{R}^2$, the appropriate semimajor axis of the hoop may be algebraically determined:

$$a_{\rm h} = \left(\frac{16\Omega^2 k_2^2 R^6}{9 I_0^2 GM} \right)^{1/3}. \tag{18}$$

Note that Equation (18) is identical to Equation (12) provided in the Supplementary Information of Batygin (2012). However, unlike Batygin (2012), we assume a fully convective T Tauri star with a polytropic index of $n = 3/2$. For such a star, the Love number and moment of inertia factor have characteristic values $I_0 = 0.21$ and $k_2 = 0.14$ (Chandrasekhar 1939).

By modeling the oblate central star as a circular wire forced by an external disk, the problem with which we are concerned here is nearly identical to that described in the previous section. Our analysis can thus proceed in much the same way, with the caveat that the inclination of the external perturber, in this case the inner disk, is no longer set to zero but maintains some constant value throughout its evolution. In orbital elements, the Hamiltonian is written as (Equation (A3) of Mardling 2010)

$$\begin{aligned} \mathcal{K}_{\rm wire} = &-\frac{1}{4}\frac{G dm_{\rm in} m_{\rm h}}{a_{\rm in}} \left(\frac{a_{\rm h}}{a_{\rm in}}\right)^2 \\ &\times \left[\frac{1}{4}(3\cos^2(i_{\rm in}) - 1)(3\cos^2(i_{\rm h}) - 1) \right. \\ &+ \frac{3}{4}\sin(2i_{\rm in})\sin(2i_{\rm h})\cos(\Omega_{\rm in} - \Omega_{\rm h}) \\ &\left. + \frac{3}{4}\sin^2(i_{\rm in})\sin^2(i_{\rm h})\cos(2(\Omega_{\rm in} - \Omega_{\rm h})) \right]. \end{aligned} \tag{19}$$

Again, we exchange orbital elements for Poincaré coordinates, integrate radially with respect to the inner disk ($a_{\rm in}$), and scale Equation (19) by the angular momentum of the stellar hoop $\Lambda_{\rm h} = m_{\rm h}\sqrt{GMa_{\rm h}}$ to find the Hamiltonian: $\tilde{\mathcal{K}}_{\rm wire} = \mathcal{K}_{\rm wire}/\Lambda_{\rm h}$. This form of the Hamiltonian given in Mardling (2010) assumes circular orbits for the disk components. The final prefactor of the Hamiltonian gives the characteristic nodal precession frequency of the stellar spin axis, which we calculate to be

$$f = \frac{3\pi}{4}\sqrt{\frac{GM}{a_{\rm h}^3}}\frac{\Sigma_0 a_0 a_{\rm x}}{M}\left(\frac{a_{\rm h}}{a_{\rm x}}\right)^3. \tag{20}$$

As mentioned in Section 3.1, Equation (12) is independent of $z_{\rm in}$. This means the inner disk inclination with respect to the binary plane, ($i_{\rm in}$), is conserved, while the inner disk node precesses at a constant rate (ω). The Hamiltonian ($\tilde{\mathcal{K}}$) is therefore a nonautonomous system with a particularly simple time dependence ($z_{\rm in} = \omega t$). The Hamiltonian can be made autonomous with a correspondingly straightforward canonical transformation into a frame precessing with the node of the inner disk. To boost into this new frame, we employ a generating function of the second kind (Morbidelli 2002),

$$G_2 = (z_{\rm h} - \omega t)\Phi, \tag{21}$$

where $\phi = (z_{\rm h} - \omega t)$ is the canonical coordinate, and the canonical momentum is determined using the relation

$$Z_{\rm h} = \frac{\partial G_2}{\partial z_{\rm h}} = \Phi. \tag{22}$$

The Hamiltonian is then transformed according to

$$\bar{\mathcal{K}} = \tilde{\mathcal{K}} + \frac{\partial G_2}{\partial t}. \tag{23}$$

Having removed the explicit time dependence, we also scale the Hamiltonian by ω so that all evolving parameters are contained in a single prefactor f/ω, and the Hamiltonian takes the form

$$\begin{aligned} \bar{\mathcal{K}} = &-\Phi + \frac{f}{\omega}\left[\frac{3}{4}\left(\frac{2}{3} - 2Z_0 + Z_0^2\right)\left(\frac{2}{3} - 2\Phi + \Phi^2\right) \right. \\ &+ (Z_0 - 1)\sqrt{Z_0(2 - Z_0)}(\Phi - 1)\sqrt{\Phi(2 - \Phi)} \\ &\left. \times \cos(\phi) + \frac{1}{4}Z_0(Z_0 - 2)\Phi(\Phi - 2)\cos(2\phi) \right]. \end{aligned} \tag{24}$$

Invoking Hamilton's equations, the evolution of the stellar spin axis is governed by the partial derivatives of Equation (24) with respect to canonical coordinates Φ and ϕ. And the stellar obliquity is defined by the dot product of the stellar and disk angular momentum vectors.

4. Obliquity Excitation

The Hamiltonian in Equation (24) is characterized by two physical timescales, the inner disk precession timescale ($2\pi/\omega$) and the stellar spin axis precession timescale ($2\pi/f$). Obliquity excitation is expected to occur when f and ω evolve such that their ratio crosses unity from above, as $f > \omega$ at early times. Using Equations (15) and (20), the ratio (f/ω) simplifies to

$$\frac{f}{\omega} = \frac{8}{3\cos(i_{\rm in})}\frac{k_2}{I}\left(\frac{R_\star}{a_x}\right)^3\left(\frac{a_x}{A_{\rm in}}\right)^{3/2}\left(\frac{A_{\rm out}}{a_x}\right)^2, \tag{25}$$

where we have substituted Equation (18) for $a_{\rm h}$ and assumed that the star is corotating with the inner edge of the inner disk, or $\Omega = \sqrt{GM/a_{\rm x}^3}$. In the case of this second substitution, we have imposed a "disk-locked" condition, in which the disk truncation radius is coincident with the radius at which the relative velocity of the stellar magnetosphere and disk material is zero (Koenigl 1991; Shu et al. 1994; Mohanty & Shu 2008). While disk-locked is an idealization that ignores the complexities of magnetic disk–star coupling, it is correct to within an order of magnitude and therefore an appropriate simplification in the context of this work.

The evolution of the characteristic timescales ($2\pi/f$ and $2\pi/\omega$) over the lifetime of the disk are shown in Figure 3. From the figure, it is clear that as the inner and outer disks dissipate, both timescales increase, but the stellar precession timescale ($2\pi/f$) is additionally dependent on stellar contraction. That is, f decreases more steeply with time than ω, and crossing is inevitable so long as $f > \omega$ in the beginning of the evolution. By setting $f/\omega = 1$ and $t = 0$, we can solve for the minimum value

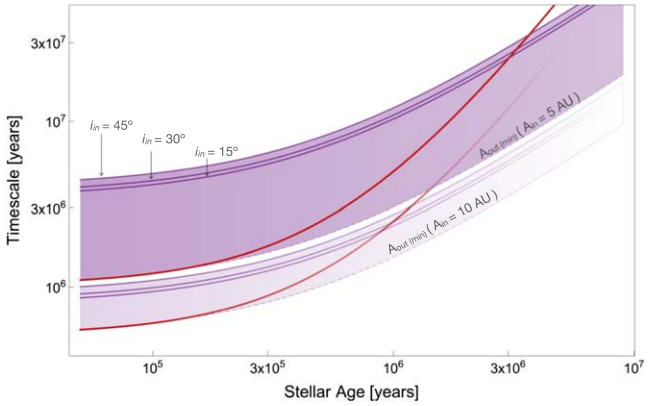

Figure 3. Evolution of timescales associated with the stellar spin axis ($2\pi/f$; red) and inner disk ($2\pi/\omega$; purple). Multiple disk geometries are illustrated. An opacity gradient is applied for an inner gap edge $A_{\rm in} = 10$ au, for which the time to resonant crossing of f and ω is shorter. The shaded purple regions describe inner disk precession for an outer gap ($A_{\rm out}$) ranging from 80 au to $A_{\rm out(min)}$ determined by Equation (26). Solid purple contours identify the boundaries of ($2\pi/\omega$) for $i_{\rm disk} = 15°$, 30°, and 45°.

of the outer edge of the disk gap ($A_{\rm out(min)}$) for which obliquity excitation can be expected to occur,

$$A_{\rm out(min)} \approx 33\ {\rm au}\sqrt{\cos(i_{\rm in})}\left[\frac{A_{\rm in}}{\rm au}\right]^{1/4}\left[\frac{M_\star}{M_\odot}\right]^{-1/4} \times\left[\frac{a_0}{\rm au}\frac{\Sigma_0}{2\times10^4\ {\rm g\,cm^{-3}}}\right]^{-1/2}\left[\frac{R_0}{4R_\odot}\right]^{3/2} \times\left[\frac{B_{\rm s}}{0.1{\rm T}}\right]\left[\frac{\tau_{\rm acc}}{0.5\ {\rm Myr}}\right]^{1/2}. \quad (26)$$

Note that $A_{\rm out(min)}$ is consistent with the angular momentum hierarchy outlined in Section 2, remaining above 40 au for $i_{\rm in} \leqslant 50°$ and 63° when $A_{\rm in} = 5$ and 10 au, respectively. Additionally, as Figure 3 illustrates, for all relevant disk parameters, f/ω crosses unity well within a maximum disk lifetime of $\sim 10^7$ yr.

Having demonstrated that the relevant timescales are consistent with obliquity excitation, we can use the analytical framework developed in Section 3 to explore the outcome of the encounter for different system configurations. Six example evolutions are shown in Figure 4. The variable parameters compared include the disk gap bounds ($A_{\rm in}$ and $A_{\rm out}$) and the inner disk inclination ($i_{\rm in}$). In the upper panel, evolved systems have $A_{\rm in}$ set to 5 au, and in the lower panel, $A_{\rm in} = 10$ au. In both panels, dark curves indicate a disk inclination of 30° with $A_{\rm out}$ minimized according to Equation (26). Evolutions plotted in gray have $A_{\rm out}$ set to 40 au and disk inclination set according to Equation (26). For systems plotted in lighter tones, $A_{\rm out}$ is maximized according to angular momentum constraints and set to 90 au.

The initial dynamical behavior is consistent between all of the systems considered in Figure 4; early in the evolution, efficient angular momentum transport between the inner disk and star leads to gravitational coupling. The stellar spin axis trails just behind the precessing angular momentum vector of the inner disk, resulting in small oscillations in obliquity.

As the systems evolve and the ratio of disk and stellar precession frequencies (f/ω) approaches unity, they experience a distinct jump in obliquity. The amplitude of this excitation

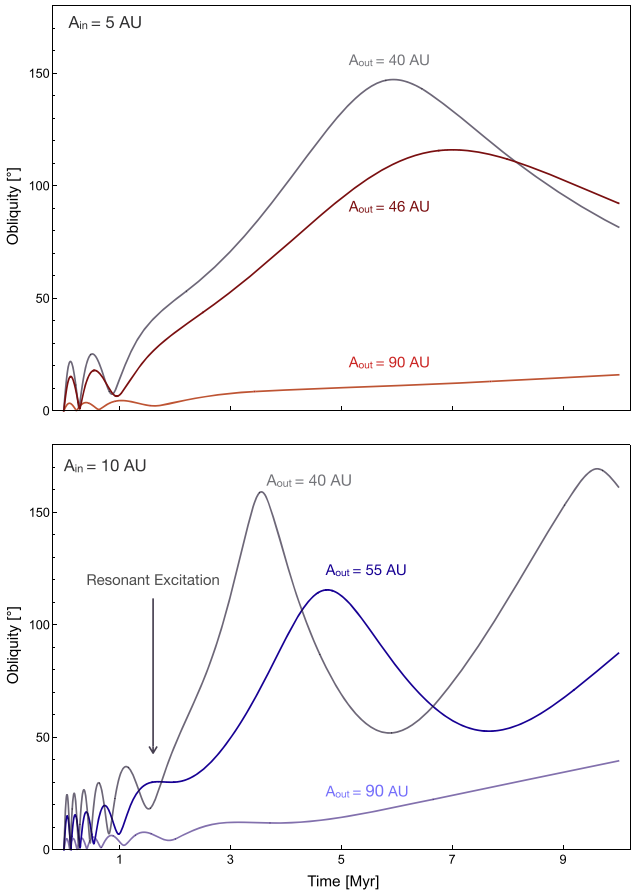

Figure 4. The obliquity evolution of the stellar spin axis was calculated by numerically solving Hamilton's equations with respect to the canonical variables Φ and ϕ and the Hamiltonian in Equation (24). The evolution of several different disk geometries is shown ($A_{\rm in} = 5$ and 10 au in red and blue, respectively). Integrations plotted in blue and red have $i_{\rm disk} = 30°$. Lighter tones differentiate integrations with $A_{\rm out} = 90$ au, and darker tones show integrations with $A_{\rm out} = A_{\rm out(min)}$. Gray curves indicate that $A_{\rm out}$ is set to 40 au, and $i_{\rm disk}$ is set by Equation (26) to 50° and 63° in the upper and lower panel, respectively.

ranges from tens of degrees to nearly 180°, where the primary factor distinguishing a large jump in obliquity from a small jump is the time of resonant encounter. By decreasing the disk gap width, we decrease the precession timescale ratio (f/ω) and the time to resonant crossing. When the excitation occurs late in the evolution, the star is significantly less oblique and the inner and outer disks have largely dissipated, resulting in significantly diminished gravitational torques and muted obliquity excitation. And while extreme obliquities can be achieved via this disk torquing mechanism, the parameters required press the resonant crossing boundary laid out in Equation (26). That is, while obliquities can clearly occur as a result of broken disk torquing, the mechanism is fundamentally less severe than the obliquities produced in the analogous binary torquing case by virtue of their occurring later in the disk lifetime.

5. Conclusion

In this work, we have identified a pathway by which obliquities may be excited in the context of a pure disk–star

system. Building from the binary torquing framework (Batygin 2012; Batygin & Adams 2013; Spalding & Batygin 2014; Lai et al. 2018), we analyze stellar spin axis forcing in the potential of a broken disk and show that large spin–orbit misalignments can be generated without invoking a binary companion. For nominal parameters, well within the observational range described by Ansdell et al. (2020) and Francis & van der Marel (2020), we show that conditions for resonant excitation are generally met.

While our results demonstrate that a misaligned, broken disk is capable of torquing the host star out of alignment, in developing our model, we have employed several simplifications in an effort to enhance the clarity of our model. In our estimation, these complicating factors will not change the overall outcome, but they are critical to note. In particular, we have assumed here that the boundary of the disk gap remains static throughout the lifetime of the disk. The origin and evolution of disk gaps remains an active area of investigation, but the radial structure is likely in flux early on in the disk lifetime (van der Marel et al. 2018, 2019). The relatively late onset of resonant excitation seen in the disk–disk torquing scenario suggests that early variation in the radial gap structure is unlikely to have a significant effect on the excitation of stellar obliquity.

Additionally, the Hamiltonian given in Equation (24) neglects nonconservative effects in the disk–disk system. Averaging of gravitational torques over the precession timescale of the stellar spin axis create a dynamical equilibrium aligned with the angular momentum vector of the outer disk. Dissipative processes, such as accretion and magnetic torquing, force the spin axis closer to this equilibrium (Batygin & Morbidelli 2011; Spalding & Batygin 2015). Interestingly, this means that even if the effects of dissipation overwhelmed the resonant excitation, the stellar spin axis would be expected to be misaligned with respect to the inner disk.

The object of this work has been to establish broken disk torquing as a viable alternative pathway to stellar obliquities. We note, however, that misalignments generated via disk torquing may differ fundamentally from their binary-generated counterparts. Because the inner and outer disks evolve along a shared trajectory, disk dissipation has significantly less impact on the overall system evolution than stellar contraction. The evolutionary track, and by extension stellar type, of the star in question thus retains an outsized role in obliquity generation. The extended contraction timescale for an M dwarf, for instance, limits the resonant crossing time to the end stages of the disk lifetime, at which point the diminished gravitational torques do not permit large obliquity excitation.

In the case of T Tauri stars explored in this work, the evolutionary track does provide an opportunity for the generation of misalignments. However, the singular dependence on the contraction timescale means that the amplitudes of obliquity excitations are largely dependent on disk gap parameters and require more tuning to achieve high amplitudes than those produced by the binary torquing mechanism. A detailed study of the ways in which the results of these two processes diverge is outside of the scope of this work but may provide avenues for future study.

We would like to thank our referee, Rosemary Mardling, whose thoughtful insights significantly improved this work. J.C.B. has been supported by the Heising-Simons 51 Pegasi b postdoctoral fellowship. M.E.M. is supported by the Graduate Fellowship for STEM Diversity. This research is based in part upon work supported by NSF grant AST 2109276. K.B. thanks the David and Lucile Packard Foundation for their generous support.

Software: pandas (McKinney 2010), IPython (Pérez & Granger 2007), matplotlib (Hunter 2007), scipy (Virtanen et al. 2020), numpy (Harris et al. 2020), Jupyter (Kluyver et al. 2016), Mathematica (Wolfram Research, Inc. 2020).

ORCID iDs

Marguerite Epstein-Martin https://orcid.org/0000-0001-9310-7808
Juliette Becker https://orcid.org/0000-0002-7733-4522
Konstantin Batygin https://orcid.org/0000-0002-7094-7908

References

Andrews, S. M., Wilner, D. J., Hughes, A. M., Qi, C., & Dullemond, C. P. 2009, ApJ, 700, 1502
Ansdell, M., Gaidos, E., Hedges, C., et al. 2020, MNRAS, 492, 572
Armitage, P. J. 2020, Astrophysics of planet formation (Cambridge: Cambridge Univ. Press)
Bate, M. R., Lodato, G., & Pringle, J. E. 2010, MNRAS, 401, 1505
Batygin, K. 2012, Natur, 491, 418
Batygin, K., & Adams, F. C. 2013, ApJ, 778, 169
Batygin, K., & Morbidelli, A. 2011, CeMDA, 111, 219
Batygin, K., Morbidelli, A., & Tsiganis, K. 2011, A&A, 533, A7
Beaugé, C., & Nesvorný, D. 2012, ApJ, 751, 119
Borucki, W. J., Koch, D., Basri, G., et al. 2010, Sci, 327, 977
Borucki, W. J., Koch, D. G., Basri, G., et al. 2011, ApJ, 736, 19
Brauer, R., Pantin, E., Di Folco, E., et al. 2019, A&A, 628, A88
Chandrasekhar, S. 1939, An introduction to the study of stellar structure (Mineola, NY: Dover Publications)
Fabrycky, D., & Tremaine, S. 2007, ApJ, 669, 1298
Facchini, S., Juhász, A., & Lodato, G. 2018, MNRAS, 473, 4459
Ford, E. B., & Rasio, F. A. 2008, ApJ, 686, 621
Francis, L., & van der Marel, N. 2020, ApJ, 892, 111
Ghosh, P., & Lamb, F. K. 1978, ApJL, 223, L83
Guerrero, N. M., Seager, S., Huang, C. X., et al. 2021, ApJS, 254, 39
Harris, C. R., Millman, K. J., & van der Walk, S. J. 2020, Natur, 585, 357
Hartmann, L. 2008, PhST, 130, 014012
Herczeg, G. J., & Hillenbrand, L. A. 2008, ApJ, 681, 594
Hillenbrand, L. A. 2008, PhST, 130, 014024
Hjorth, M., Albrecht, S., Hirano, T., et al. 2021, PNAS, 118, 2017418118
Howell, S. B., Sobeck, C., Haas, M., et al. 2014, PASP, 126, 398
Hunter, J. D. 2007, CSE, 9, 90
Kant, I. 1755, General History of Nature and Theory of the Heavens (Königsberg: Petersen)
Kaula, W. M. 1962, AJ, 67, 300
Kluyver, T., Ragan-Kelley, B., Pérez, F., et al. 2016, in Proc. of the 20th Int. Conf. on Electronic Publishing, ed. F. Loizides & B. Schmidt (Amsterdam: IOS Press), 87
Koenigl, A. 1991, ApJL, 370, L39
Lai, D. 2014, MNRAS, 440, 3532
Lai, D., Anderson, K. R., & Pu, B. 2018, MNRAS, 475, 5231
Lai, D., Foucart, F., & Lin, D. N. C. 2011, MNRAS, 412, 2790
Laplace, P. S. 1796, Exposition du système du monde (Paris: Cerie-Social)
Larwood, J. D., Nelson, R. P., Papaloizou, J. C. B., & Terquem, C. 1996, MNRAS, 282, 597
Laughlin, G., Bodenheimer, P., & Adams, F. C. 2004, ApJL, 612, L73
Lithwick, Y., & Wu, Y. 2012, ApJL, 756, L11
Mardling, R. A. 2010, MNRAS, 407, 1048
McKinney, W. 2010, in Proc. of the 9th Python in Science Conf., ed. S. van der Walt & J. Millman (Austin, TX: SciPy), 56
McLaughlin, D. B. 1924, ApJ, 60, 22
Mestel, L. 1963, MNRAS, 126, 553
Mohanty, S., & Shu, F. H. 2008, ApJ, 687, 1323
Morbidelli, A. 2002, Modern celestial mechanics: aspects of solar system dynamics (Milton Park: Taylor & Francis)
Morton, T. D., & Winn, J. N. 2014, ApJ, 796, 47

Murray, C. D., & Dermott, S. F. 1999, Solar system dynamics (Cambridge: Cambridge Univ. Press)
Nagasawa, M., Ida, S., & Bessho, T. 2008, ApJ, 678, 498
Naoz, S., Farr, W. M., Lithwick, Y., Rasio, F. A., & Teyssandier, J. 2011, Natur, 473, 187
Nealon, R., Dipierro, G., Alexander, R., Martin, R. G., & Nixon, C. 2018, MNRAS, 481, 20
Pérez, F., & Granger, B. E. 2007, CSE, 9, 21
Rossiter, R. A. 1924, ApJ, 60, 15
Shu, F., Najita, J., Ostriker, E., et al. 1994, ApJ, 429, 781
Siess, L., Dufour, E., & Forestini, M. 2000, A&A, 358, 593
Spalding, C., & Batygin, K. 2014, ApJ, 790, 42
Spalding, C., & Batygin, K. 2015, ApJ, 811, 82
Tremaine, S. 1991, Icar, 89, 85
van der Marel, N., Dong, R., di Francesco, J., Williams, J. P., & Tobin, J. 2019, ApJ, 872, 112
van der Marel, N., Williams, J. P., & Bruderer, S. 2018, ApJL, 867, L14
Virtanen, P., Gommers, R., Oliphant, T., et al. 2020, NatMe, 17, 261
Winn, J. N., Fabrycky, D., Albrecht, S., & Johnson, J. A. 2010, ApJL, 718, L145
Winn, J. N., & Fabrycky, D. C. 2015, ARA&A, 53, 409
Winn, J. N., Noyes, R. W., Holman, M. J., et al. 2005, ApJ, 631, 1215
Wolfram Research, Inc. 2020, Mathematica, v13.0, https://www.wolfram.com/mathematica
Wu, Y., & Murray, N. 2003, ApJ, 589, 605
Zanazzi, J. J., & Lai, D. 2018, MNRAS, 477, 5207
Zhu, Z. 2019, MNRAS, 483, 4221